

www.acsami.org Research Article

# Submicron Metal 3D Printing by Ultrafast Laser Heating and Induced Ligand Transformation of Nanocrystals

Chinmoy Podder, Xiangtao Gong, Xiaowei Yu, Wan Shou, and Heng Pan\*



Cite This: https://doi.org/10.1021/acsami.1c10775



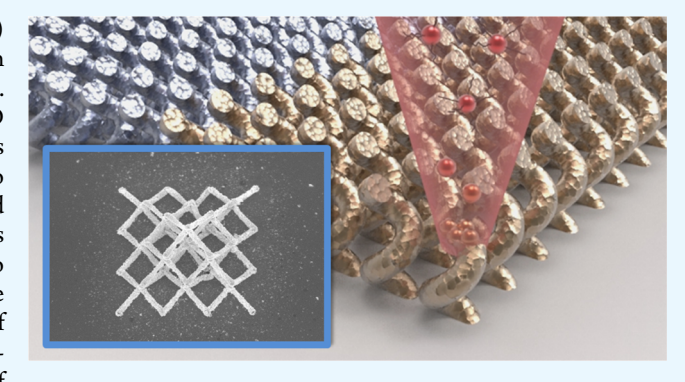
**ACCESS** 

III Metrics & More



Supporting Information

ABSTRACT: Currently, light-based three-dimensional (3D) printing with submicron features is mainly developed based on photosensitive polymers or inorganic-polymer composite materials. To eliminate polymer/organic additives, a strategy for direct 3D assembly and printing of metallic nanocrystals without additives is presented. Ultrafast laser with intensity in the range of  $1\times 10^{10}$  to  $1\times 10^{12}$  W/cm² is used to nonequilibrium heat nanocrystals and induce ligand transformation, which triggers the spontaneous fusion and localized assembly of nanocrystals. The process is due to the operation of hot electrons as confirmed by a strong dependence of the printing rate on laser pulse duration varied in the range of electron—phonon relaxation time. Using the developed laser-induced ligand transformation (LILT) process, direct printing of



3D metallic structures at micro and submicron scales is demonstrated. Facile integration with other microscale additive manufacturing for printing 3D devices containing multiscale features is also demonstrated.

KEYWORDS: 3D printing, submicron, femtosecond laser, ligand, nanocrystals, hot electron, microadditive manufacturing

#### ■ INTRODUCTION

Additive manufacturing (AM), initially developed as a stereolithography technique, has revolutionized conventional manufacturing technologies by providing freedom of fabrication of arbitrarily complex three-dimensional (3D) structures. Since its invention in the mid-1980s, the printing resolution has improved and the range of applicable materials has been expanded. There are several popular AM techniques that cover a range of materials and feature sizes from hundreds of microns to submicron scales. Fused deposition modeling (FDM) can print thermoplastics with the feature  $\sim 200 \ \mu \text{m}$ ; direct metal deposition (DMD) is a powder jet technique that can be used to build, repair, and reconfigure macroscale metal components.<sup>2</sup> Selective laser sintering (SLS) uses a laser to sinter powdered metal or polymer materials for rapid prototyping or low-volume production of component parts and features down to  $\sim 100 \ \mu m$  can be fabricated by micro-SLS.<sup>3</sup> Microstereolithography including two-photon polymerization<sup>4</sup> can achieve high spatial resolution (down to ~100 nm) in a 3D manner. Direct ink writing (DIW) is an extrusion-based process<sup>5</sup> capable of printing 3D feature down to  $\sim$ 50  $\mu$ m and minimum two-dimensional (2D) feature ~250 nm using solgel inks. Electrodynamic jet printing is an emerging AM technique with resolution down to submicron. Metal and polymer structures down to 1  $\mu$ m<sup>6</sup> and pillars ~120 nm have been printed.7

Among various AM techniques, 3D printing of micro/ nanostructures is important because of their diverse applications, especially in electronics, 8,9 optics, 10 and medical fields. 11 A wide range of materials including ceramics, 12-15 polymers, 4 composite, 16 semiconductors, 17 and metals 18 have been used for this purpose. Today, most of the commercially available metal AM processes are at the macroscale, while direct printing true 3D metal structures with submicron resolution without involving organic additives is still under investigation. Metal micro/nanofabrication is of high interest in printable electronics, 8,9,19,20 microelectromechanical systems, <sup>21</sup> nanophotonics, <sup>22,23</sup> and biomedical devices. <sup>24</sup> In particular, vertical submicron metallic pillar arrays have found interesting applications in the energy, catalysis, and biomedical fields  $^{25-27}$  due to their unique mechanical, optical, and electronic properties. The most notable biorelated applications are probe-based sensing of cell activity,<sup>28</sup> antibacterial surfaces, 29 intracellular delivery, and intracellular electrical stimulation and sensing.<sup>30</sup> Currently, manufacturing of submicron pillars requires multistep lithography, deposition,

Received: June 9, 2021 Accepted: August 13, 2021



**ACS Applied Materials & Interfaces** 

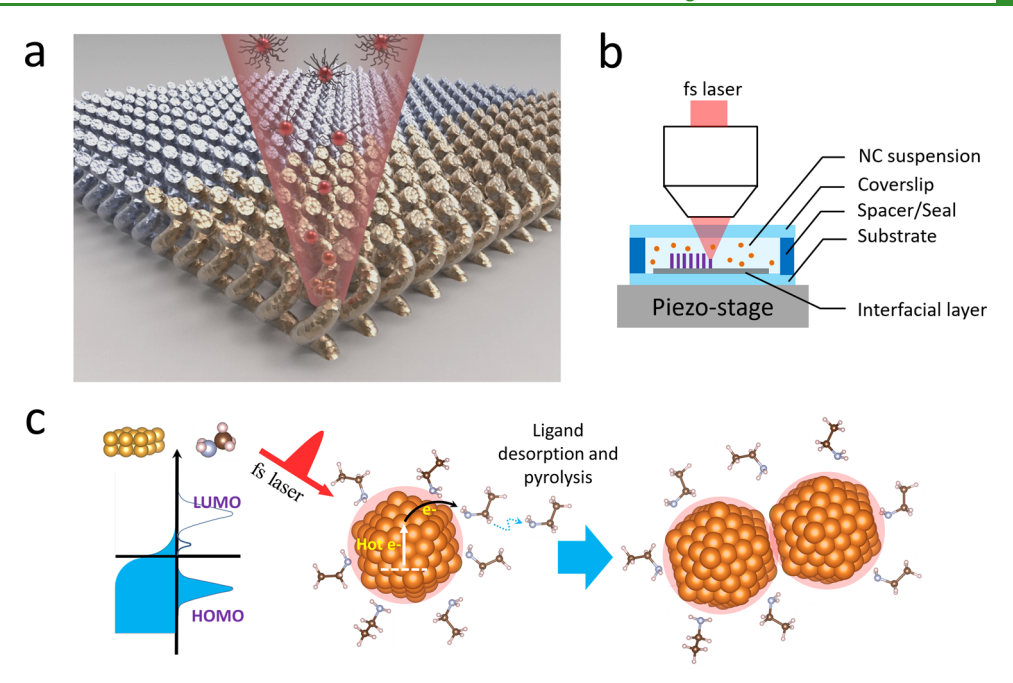


Figure 1. Laser-induced ligand transformation process for 3D printing. (a) Illustration of the laser 3D metal printing process. (b) Experimental configuration of the laser 3D metal printing process. (c) Ultrafast laser excitation of nanocrystals capped by oleylamine (OA) ligands and induced ligand transformation and nanocrystal fusion.

plasma etching, and templating,<sup>27</sup> which is expensive and less controllable. A direct 3D metal printing process with submicron features would be highly desirable.

Massive amount of research on 3D metal printing focuses on features >10  $\mu\rm m$ , such as inkjet printing,  $^{31}$  aerosol jet printing,  $^{32}$  microselective laser sintering,  $^{3}$  and laser chemical vapor deposition,  $^{33}$  or 1–10  $\mu\rm m$ , such as direct ink writing  $^{34}$  and laser-induced forward transfer.  $^{35-38}$  Several works with sub- $\mu\rm m$  features have been reported, including electrohydrodynamic printing,  $^{7}$  laser electrophoretic deposition,  $^{39}$  and localized electroplating,  $^{40,41}$  which all require conductive or semiconductive substrates. Focused electron/ion beam-induced deposition could reach tens of nm resolution  $^{42}$  at a cost of focused ion beam/scanning electron microscope (SEM/FIB) equipment.

Laser-direct writing (laser-DW) is an affordable and versatile method for high-precision 3D printing. Currently, laser-DW 3D printing with submicron features is mainly developed based on resins consisting of photosensitive polymers or inorganicpolymer composite materials. Laser-induced photoreduction of the metal salt is a well-known method for metal printing with features ~180 nm.  $^{43-47}$  To achieve sub- $\mu$ m features and true 3D structuring, it is crucial to involve organic additives, such as polymer matrix<sup>44</sup> for mechanical support, photosensitizing dye to reduce laser intensity, 48 and/or surfactants 45,46 to suppress excessive crystal growth. However, the use of organic additives results in less effective metal components and low electrical conductivity in final structures. Cao et al. reported a freestanding pillar ~180 nm in diameter; however, no electrical conductivity was reported. 46 Blasco et al. achieved ~2% bulk electrical conductivity, while demonstrated structures are in microscales (not submicron).<sup>47</sup> Barton et al. reported high electrical conductivity of printed metallic structures (~25% of bulk conductivity) by optimizing the surfactants, and 2D and 2.5D structures were demonstrated in this work.<sup>45</sup> Until today, it is still challenging to achieve true 3D structure (e.g.,

overhanging structures  $^{47}$ ), sub- $\mu$ m resolution,  $^{45,46}$  and high electrical conductivity  $^{43,45,47}$  simultaneously using the photoreduction method based on organic additive resins (Supporting information, Table S1). One solution to remove organic residuals is through post-processing. Recently, two-photon lithography is followed by pyrolysis (700 °C) to print hierarchical 3D structures with resolution 25–100 nm. However, the high-temperature post-processing creates significant deformation and poses challenges in process integration. Therefore, it is desirable to develop an organic additive-free and low-temperature process for conductive 3D metal printing with submicron resolution.

In recent years, we have witnessed significant progress in using ligand-capped nanoparticles (inks) for low-temperature fabrication of metals with conductivity comparable to bulk values by removing or transforming ligands. In ligand-capped nanoparticle ink, the functional metal is fabricated by nanoparticle sintering or coalescence instead of metal ion reduction and crystal growth. Continuous-wave (CW) laser radiation was employed for sintering Au nanoparticles after deposition, and a continuous film with electrical conductivity  $\sim$ 17% of the bulk value can be fabricated. 50,51 Fast and ultrafast laser sintering of nanoparticles were demonstrated with minimized thermal diffusion on the polymeric substrate for the picosecond pulsed laser irradiation 52 and minimized lateral thermal diffusion for the femtosecond laser sintering of submicron 2D features.<sup>53</sup> However, all of these works concentrate on microstructures or sub-µm 2D structures. 34,50,53-57 Here, we report using a femtosecond laser to induce highly localized, nonthermal ligand transformation and self-fusion of nanocrystals for sub-\mu m 3D printing. A femtosecond laser with adjustable repetition rates (120 KHz-27 MHz) was used in this process. The low repetition rate is critical in facilitating 3D printing in the solvent by avoiding heat accumulation and bubble formation.<sup>58</sup> This process does not require organic additives or designed

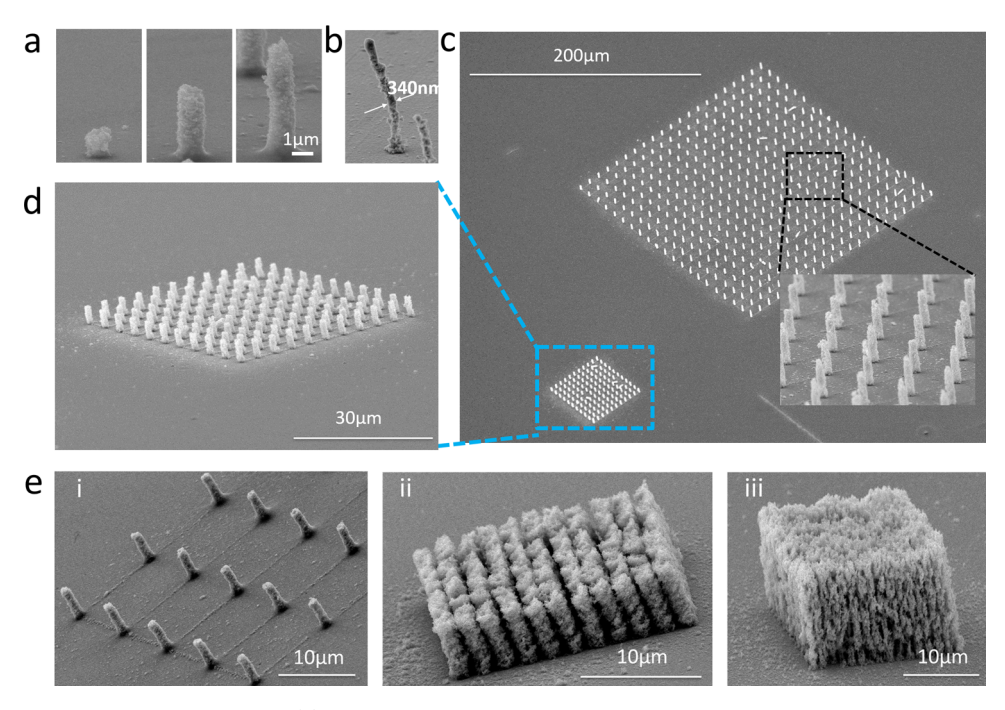


**Figure 2.** 2.5D products of the printing method. (a) SEM image of a free-standing pillar printing with 0.5, 2, and 3 s laser dwell time. (b) SEM image of a single pillar with the 340 nm diameter. (c) SEM image of large-scale printed pillar arrays. (d) SEM image of small-scale printed pillar arrays. (e, i) SEM image of the pillar array showing 11.5  $\mu$ m pillar-to-pillar gap, (ii) SEM image of the pillar array showing 1  $\mu$ m pillar-to-pillar gap, and (iii) SEM image of the 3D block (<1  $\mu$ m pillar-to-pillar gap).

photosensitive ligands<sup>59</sup> and is applicable to common ligands (such as oleylamine, a versatile ligand widely used in encapsulating metals, semiconductors, and ceramic nanoparticles<sup>60</sup>). Furthermore, it is shown that this process can be easily integrated with other additive manufacturing processes facilitating 3D printing containing multiscale features.

## ■ RESULTS AND DISCUSSION

Laser-Printing Process and Setup. A schematic of the 3D printing process is presented in Figure 1a. A femtosecond pulsed laser (1030 nm wavelength, ~700 fs pulse width) was focused by a high numerical aperture (NA = 1.3) oil immersion objective to induce 3D printing of oleylamine (OA)-capped gold nanocrystals (3-4 nm particle size, 0.2 wt % in xylene or a mixture of xylene and terpineol) in a sealed chamber. The chamber was mounted on a three-axis piezoelectric stage. The laser peak intensity  $I_0$  is in the range of 1 × 10<sup>10</sup> to 1 × 10<sup>12</sup> W/cm<sup>2</sup>, wherein  $I_0 = \frac{2E_p}{\tau} \frac{1}{\pi w_0^2}$  is the laser intensity at the center of the laser spot,  $E_p$  is the laser energy per pulse (laser power/repetition rate),  $\tau$  is the laser pulse duration, and  $w_0 = 0.6\lambda/NA$  is the radius of the diffractionlimited laser spot. When the laser pulses excite the ligandcapped nanocrystal inside solution, the ligands are transformed enabling controlled fusion and 3D printing of nanocrystals (Figure 1c).

To initialize printing and promote adhesion of the printed structures on a glass substrate, an interfacial layer (IL) was employed and prepared by spin-coating gold NC ink (25 wt % in xylene) on the substrate followed by hot-plate annealing at  $100-200~^{\circ}\text{C}$  for 1 h (Figure 1b). Without IL, the printing was hard to initiate due to the lack of adhesion and anchoring sites on glass substrates. It is found that the interfacial layer annealed at  $100-200~^{\circ}\text{C}$  is optimal for this purpose, since such

films provide anchoring sites to initiate the printing process while maintaining nonpercolating and relatively transparent at the laser wavelength. It is worth mentioning that since interfacial layers are solution-printed, they can be integrated as part of the printing process and used as functional components after being patterned and annealed, as will be demonstrated.

2.5D and 3D Microstructure Printing. Microscale and submicron free-standing pillars can be printed by dwelling the laser on top of the interfacial layer (Figure 2a,b). With the 710 kHz repetition rate and laser power ~0.8 mW (laser peak intensity  $I_0 \sim 4.54 \times 10^{11} \text{ W/cm}^2$ ), 3D pillars ( $\sim 1 \mu \text{m}$ diameter) of different heights (up to a few microns) were printed, as shown in Figure 2a with the printing rate  $\sim 3 \mu \text{m/s}$ . The smallest free-standing pillar is ~340 nm in diameter, which is achieved by using the 5.4 MHz repetition rate and  $\sim$ 0.6 mW (laser peak intensity  $I_0 \sim 4.47 \times 10^{10}$  W/cm<sup>2</sup>, Figure 2b). The pillar diameter is considerably smaller than the diffraction-limited laser spot  $2w_0 = 1.2\lambda/NA = 950$  nm. Largescale arrays of micropillars of gold electrodes were printed (Figure 2c) with raster scan mode of the piezoelectric stage (Movie S1). The larger array in Figure 2c consists of 400 pillars with each having  $\sim$ 5  $\mu$ m height and  $\sim$ 1.5  $\mu$ m diameter. Figure 2e shows pillar arrays with different pillar-to-pillar gaps.

To demonstrate that this method is capable of printing true 3D geometries, various 3D structures were fabricated (Figure 3). The piezoelectric stage was moved along the desired direction with controlled speed to print tilted pillars with different angles (Figure 3a(i-iv)). Submicron overhanging structure (~800 nm) is possible without any support (Figure 3b). Various hierarchical structures can be printed suggesting applications for mechanical metamaterials (Figure 3c-e, Movie S2). The technique is then used to print customized 3D devices containing multiscale features. The technique is first used to print metal periodic structures on an optical fiber

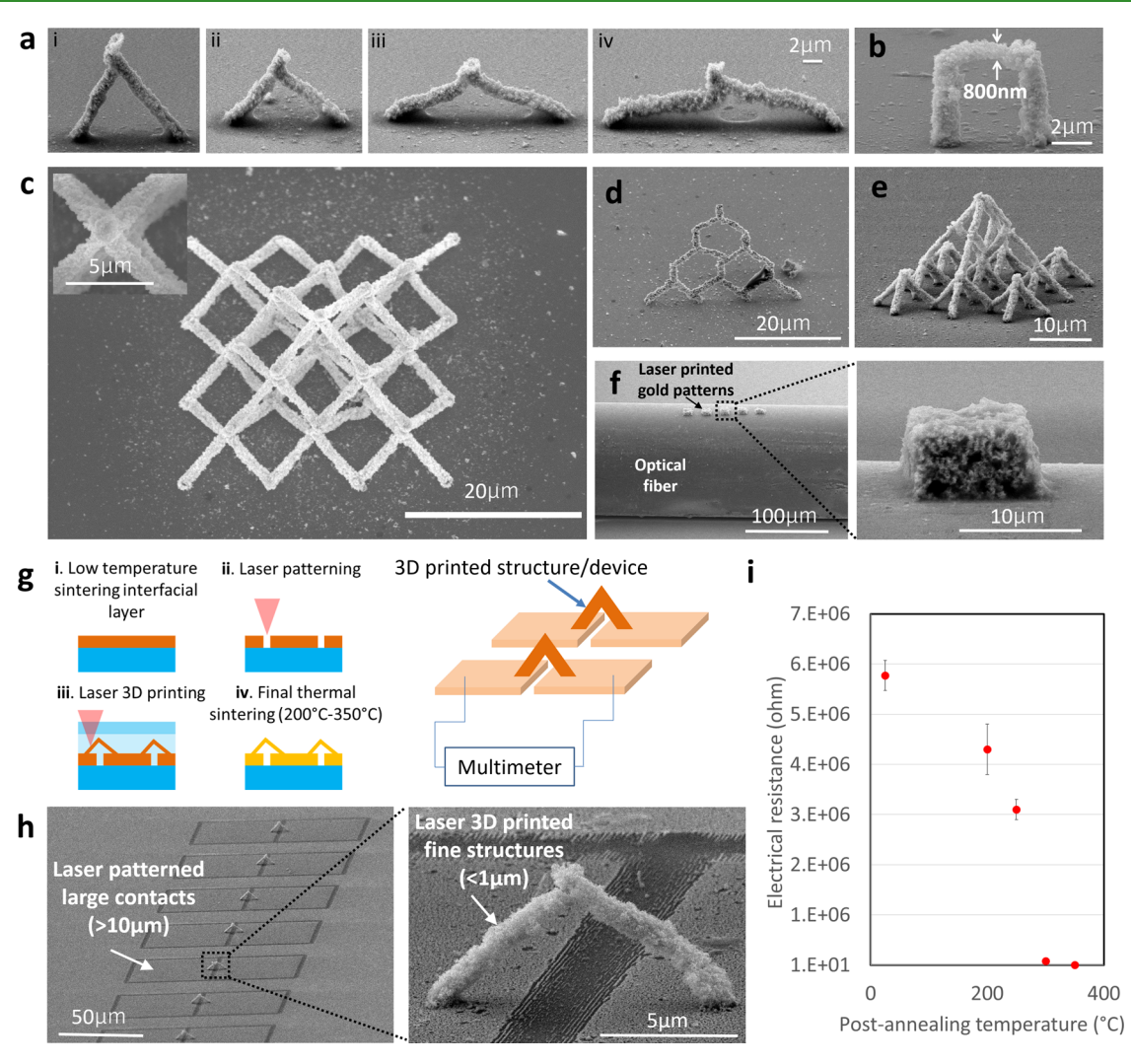
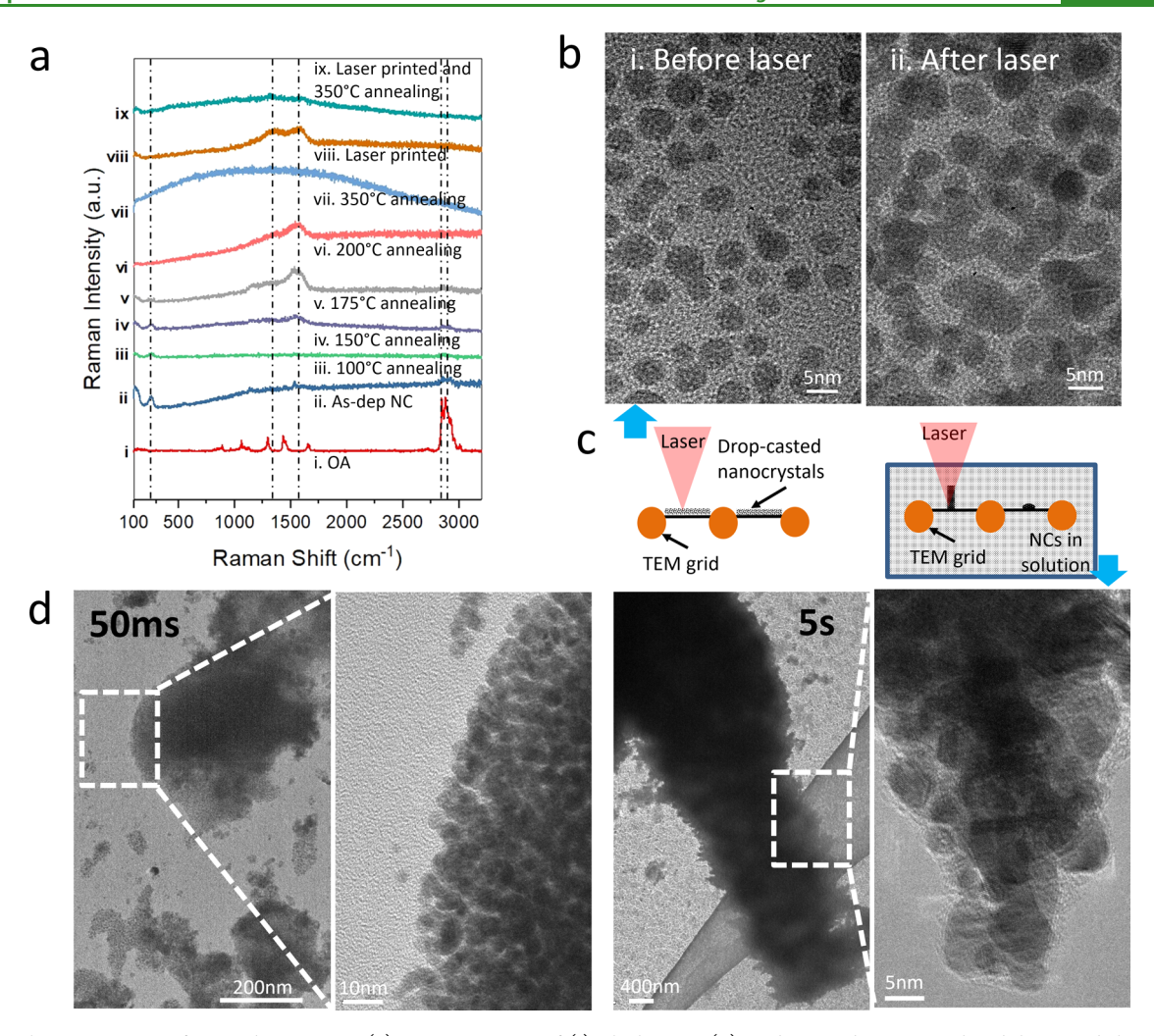


Figure 3. Complicated 3D structures printed. (a) SEM image of printed pillars tilted with various angles. (b) SEM image of the submicron overhanging structure. (c–e) Hierarchical structures for mechanical metamaterials. (f) Printed periodic gold patterns on optical fibers for fiber sensors. (g) Scheme to print 3D devices integrating submicron and microscale features and the printed device for electrical resistance measurement. (h) Example device with multiscale components (laser-patterned contacts >10  $\mu$ m and laser-printed submicron 3D structures). (i) Electrical resistance was measured using the printed 3D structures and contact pads.

with the diameter ~150  $\mu$ m, which could be used to enhance or enable new sensing capabilities for fiber sensors (Figure 3f). Figure 3g illustrates the scheme to print a 3D device integrating microscale features with sub- $\mu$ m 3D components. The spin-coated interfacial layer was annealed at 100 °C and laser-micromachined into microscale contact pads. 3D submicron structures were then printed on the patterned interfacial layer. The entire structures were annealed at 200–350 °C for 10 min. The densification of the 3D structure upon annealing is evident by a reduction in diameter and resistance (Figures 3i and S1). To determine the electrical conductivity, 2D conductors, as shown in Figure S2, were fabricated using a similar approach and the conductivity is found to be ~2 × 10<sup>6</sup> S/m (~5% of the bulk value) after annealing at 350 °C for 10 min.

Raman and Transmission Electron Microscopy (TEM) Characterization. To understand the microscopic aspects of the laser-printing process, Raman spectra as measured from oleylamine (OA), as-deposited (spin-coated) nanocrystal film, the nanocrystal film annealed at different temperatures, laser-printed structures, and laser-printed structures followed by

thermal annealing are shown in Figure 4a. The spectrum for OA exhibits peaks at 890, 1065, 1297, 1456, 1658, and 2800-3000 cm<sup>-1</sup>. These correspond to C-C stretching and R-NH<sub>2</sub> wagging, C-N stretching, -CH2 twisting, -CH2 scissor with asymmetric bending, dialkyl C=C, C-H vibration, respectively. The spectrum for as-deposited NC film exhibits obvious peaks at 261 and 2800-3000 cm<sup>-1</sup>. The peak at 261 cm<sup>-1</sup> is likely related to the Au-N bond. The rest of the OA peaks are very weak in the NC film except the characteristic C-H vibration peak. Thus, the presence of the Au-N bond and C-H vibration peaks confirms OA as the ligand on the NCs. The NC film under ambient thermal annealing starts to show a gradual decrease in the Au-N bond and C-H vibration peaks (from 100 °C up to 200 °C) along with a gradual increase of a new peak around 1560 cm<sup>-1</sup>, corresponding to the G-band (graphitic). The peak evolutions indicate that the ligand started to thermally desorb (disappearance of the Au-N bond) and transform (disappearance of the C-H vibration peak). The spectrum of the NC film annealed at 350 °C shows no obvious G-band. It is likely that the formation of the conductive/reflective metal film significantly reduces the



**Figure 4.** Characterization of printed structures. (a) Raman spectra of (i) oleylamine, (ii) as-deposited nanoparticle ink layer and the same layer annealed at (iii) 100 °C, (iv) 150 °C, (v) 175 °C, (vi) 200 °C, (vii) 350 °C, (viii) laser-printed structures, and (ix) laser-printed structures after ambient annealing at 350 °C. (b) TEM image of nanocrystals before (i) and after (ii) laser irradiation. (c) Schematics of sample preparations on TEM grids. (d) TEM images taken from laser-printed structures after various dwell times.

signature of transformed ligands. In contrast, the spectrum for laser-printed (710 kHz, 0.5 mW, NA = 1.3, peak intensity 2.84  $\times$   $10^{11}$  W/cm²) structures, the peak at 261 cm $^{-1}$  is absent and two new broad peaks appear in the 1350 cm $^{-1}$  (D or disorder band) and 1560 cm $^{-1}$  (G-band) region, which can be attributed to desorption (no Au–N bond present) and pyrolysis (presence of both D and G bands) of the long chain of OA. The spectrum for the thermally annealed laser-printed structure shows weak D and G bands, suggesting that residual carbons associated with the laser-transformed chain remain in the structure annealed at  $\sim\!350\,^{\circ}\mathrm{C}$ .

A representative high-resolution TEM image of the OA-capped nanocrystals before and after laser irradiation is presented in Figure 4b. Figure 4b(i) suggests that before laser irradiation, the nanocrystals are close-packed and isolated from each other due to the steric repulsion of the encapsulating ligands. Figure 4b(ii) suggests that after laser irradiation (NA = 0.46 objective, 710 kHz, 2.75 mW laser power,  $I_0 \sim 2.0 \times 10^{11}$  W/cm², 1 s dwell time) on those particles, coalescence and self-fusion occur among these particles. The limited grain growth of these fused particles suggests that a very controllable coalescence is possible without significant coalescence as in conventional thermal sintering. We then print pillars directly

on the sputtered gold/SiO<sub>2</sub> membrane on the transmission electron microscopy grid to analyze the atomic level microstructure of laser-printed materials. Figure 4d displays a bright-field TEM image taken from laser-printed structures after various dwell times. Multiple coalesced grains with a mean size of  $\sim$ 10 nm can be observed after laser printing. The electron diffraction pattern taken from the region shows representative gold structures (Figure S3).

Understanding the Transport during Laser–NC Interaction and Printing Mechanism. It is hypothesized that OA ligands undergo desorption and pyrolysis upon laser excitation, which reduces the original steric repulsion between NCs inside the laser voxel and results in fusion and printing of NC (Figure 1a). Considering the averaged laser intensity  $\sim 0.1-0.2 \text{ MW/cm}^2$  in this work, laser trapping is unlikely to play an important role. To trap nanocrystals, about two orders of magnitude higher laser intensity  $^{61,62}$  are needed to overcome the diffusion driven by thermal energy  $k_BT$ . Dedicated studies on the movement of nanocrystals will be carried out in the future to evaluate/confirm the effects of focused laser irradiation/heating on nanocrystal transport. As illustrated in Figure 1, the laser voxel is overlapping with the target structure (or IL on the substrate) during the printing.

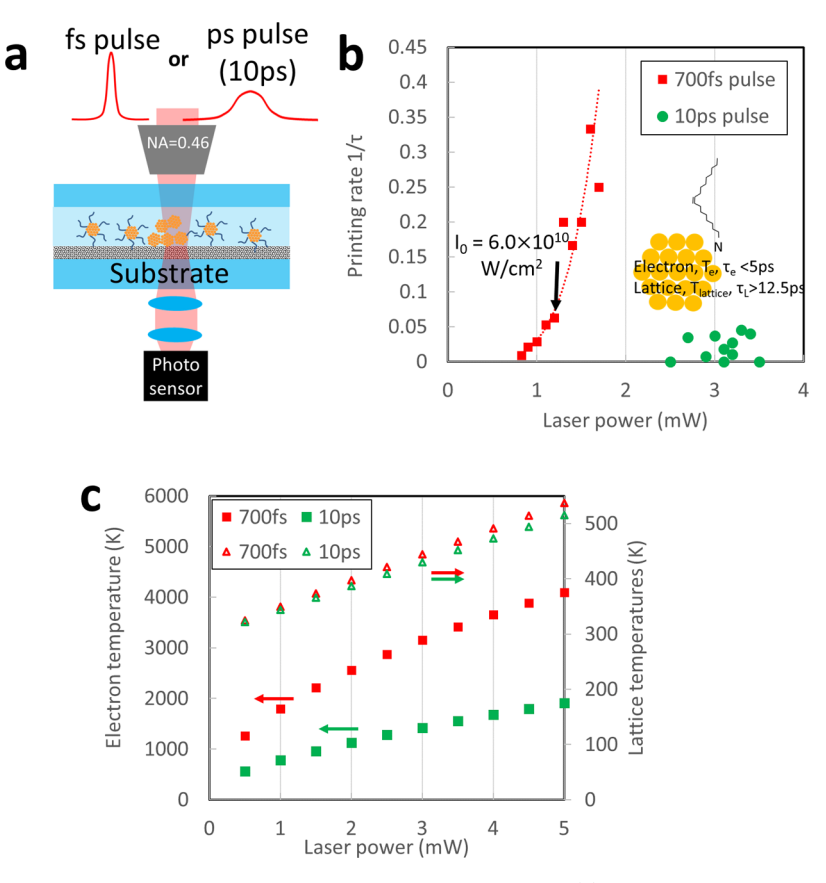


Figure 5. Hot-electron-driven ligand transformation and nanocrystal fusion mechanism. (a) Experimental configuration for the pulse duration study (the laser pulse width is tunable from  $\sim$ 700 fs to  $\sim$ 10 ps) and the measured printing rate as a function of laser power for each pulse width. (b) Obtained printing rates (estimated from optical transmission evolution) indicate that the laser power threshold to initiate NC printing is higher for laser with  $\sim$ 10 ps pulse than that with  $\sim$ 700 fs pulse. (c) Calculated peak electron temperature and lattice temperature by a three-temperature model for  $\sim$ 700 fs pulse and  $\sim$ 10 ps pulse, respectively (focusing lens NA = 0.46).

The irradiated Au nanocrystals diffuse within the laser voxel and some of them reach and attach to the target structure, which initiates and maintains the printing process. The key to the success of this printing process is that the target structure (previously printed structure or the interfacial layer on the substrate) consists of partially fused nanocrystals, which is not conductive or reflective when printed (therefore relatively transparent to printing laser), which allows printing laser to overlap with the target without causing significant heating and crystal growth.

The laser-induced ligand desorption and pyrolysis can be triggered by one of the two general mechanisms: lattice thermal heating-mediated process or hot-electron-driven processes. 63,64 In the thermal heating process, ligand reaction is mediated by lattice heating, while in the hot-electron-driven process, the coupling of laser-heated electrons (in the gold core) to the ligand motion plays an essential role. To determine the mechanism, laser pulse duration was varied in the range of electron-phonon relaxation time (from ~700 fs to ~10 ps, Figure S4) to determine its effects on the laserinduced printing rate. Figure 5a shows the printing rate ( $\sim 1/\tau$ , with  $\tau$  be the time for transmission reduces to 95%, Figure S5) versus laser power for the two pulse durations. The printing rates are considerably lower for ~10 ps pulses as compared to ~700 fs pulses at same laser powers. The lifetime of hot electron  $\tau_{\rm e}$  due to electron—phonon relaxation was found to be ~1 ps at low laser excitation intensity and ~5 ps at higher intensity. 65 In contrast, the lattice thermal relaxation time  $\tau_{\rm L}$ 

can be estimated by  $\frac{C_L D_p}{6G}$  for small nanocrystals, where  $C_L$  is the volumetric heat capacity of gold,  $D_p$  is the nanoparticle diameter, and G is the interfacial conductance at the lattice/ ligand interface. In general, G is in the range  $10-100 \text{ MW/m}^2$ K, and the particle used is 3-5 nm in diameter. The estimated thermal relaxation time  $\tau_L$  is ~33.2 ps (G = 50 MW/m<sup>2</sup> K,  $D_p$ = 4 nm), which is consistent with the recently reported lattice thermal relaxation time  $\tau_{\rm L}$  = 68 (±54) ps and  $G \sim 40~{\rm MW/m^2}$ K<sup>66</sup> for similar OA-capped gold nanocrystals. Since the range of pulse duration change (from 700 fs to 10 ps) overlaps with  $\tau_{\rm e}$  and is shorter than  $\tau_{\rm L}$ , the pulse duration change is expected to have more impact on the maximum electronic temperature reached at a certain laser fluence than lattice temperature. It is then inferred that femtosecond laser-induced ligand transformation is mainly mediated by hot electrons with a possible contribution from lattice heating.

To further illustrate the contributions from various carriers, a three-temperature (3-T) model was employed to calculate transients of the electron, lattice, and ligand temperatures<sup>63</sup>

$$\gamma T_{\rm e} \frac{{\rm d}T_{\rm e}}{{\rm d}t} = -g(T_{\rm e} - T_{\rm L}) + \frac{3Q_{\rm abs}(T_{\rm e})I(t)}{2D_{\rm p}}$$
 (1)

$$C_{\rm L} \frac{{\rm d}T_{\rm L}}{{\rm d}t} = g(T_{\rm e} - T_{\rm L}) - \frac{6G}{D_p} (T_{\rm L} - T_{\rm Ligand})$$
 (2)

$$\frac{\mathrm{d}T_{\mathrm{Ligand}}}{\mathrm{d}t} = \frac{A_{\mathrm{surf}}G}{C_{\mathrm{Ligand}}} (T_{\mathrm{L}} - T_{\mathrm{Ligand}}) \tag{3}$$

wherein  $T_{\rm e}$  is the temperature of the electron,  $T_{\rm L}$  is the temperature of the lattice,  $T_{\rm Lignad}$  is the temperature of the ligand, G is the thermal conductance between the ligand and

NC (
$$G \sim 50 \text{ MW/m}^2 \text{ K}$$
), and  $I(t) = \frac{2E_p}{\tau_p} \frac{1}{\pi w_0^2} \exp\left(-2.77 \frac{t^2}{\tau_p^2}\right)$  is

the temporal evolution of laser intensity at the laser spot center. Note that the ligand temperature calculation (eq 3) has not considered the ligand-electron coupling in its current form. Detailed 3-T model parameters are in the Supporting information (Table S2). Figure 5c shows the computed temperatures for laser pulse duration  $\tau_p = 700$  fs and 10 ps. The pulse duration difference causes ~10-20 K difference in lattice temperature. The difference in lattice temperatures slightly offset the laser power (up to ~0.5 mW) needed for the 10 ps laser pulse to reach the same peak lattice temperature achieved by 700 fs pulse. However, this offset solely is insufficient to explain the laser power threshold offset, as observed experimentally (Figure 5b). On the other side, a significant difference in electron temperatures can be seen in Figure 5c. This observation indicates that the printing process has a strong correlation with electron temperature. It has been reported that the hot electron could couple to the vibration of ligand molecules. <sup>66,67</sup> We hypothesize that the ligand heating due to electron-ligand coupling is the mechanism responsible for ligand transformation, which correlates strongly with electron lifetime.

It is worth mentioning that the nanocrystal also exhibits a slower and nanosecond relaxation time scale due to thermal relaxation to the surrounding. It is found that the slower thermal relaxation can take up to a few hundred nanoseconds. To avoid heat accumulation, the laser repetition rates adopted in this work were from 710 kHz to 5.4 MHz, which correspond to 1400 to 185 ns interpulse separation time. With the relatively low repetition rate, adverse effects (e.g., overheating and bubble formation) due to heat accumulation are minimized and 3D printing in the solvent becomes possible, which enables current technology.

# CONCLUSIONS

Direct 3D metal printing has been mainly focused on macroscales. Here, a strategy for direct 3D printing of metal structures with features at micro- and submicron scales is presented. Transient heating of nanocrystals with laser intensity in the range of  $1\times 10^{10}$  to  $1\times 10^{12}$  W/cm² induces ligand transformation and spontaneous fusion of nanocrystals. The process is due to the operation of hot electrons as confirmed by a strong dependence of the printing rate on laser pulse duration varied in the range of electron—phonon relaxation time. The electronic driven process facilitates nonthermal nanocrystal sintering and printing within the solvent. A variety of 3D structures including submicron overhanging features and hierarchical structures were demonstrated.

To implement this technique for energy, catalysis, and biomedical applications, several technical issues are to be addressed in future works. It is critical to scale up printing throughput and increase the volume or area of the printed structures significantly. High-throughput laser processing by projection or high-speed scanning will be implemented. The

nanocrystal depletion resulted from high-throughput printing needs to be remedied by supplying new inks to the chamber during printing. The 5% bulk electrical conductivity achieved currently is associated with residual carbon. For this reason, modest mechanical properties of the printed structure are also anticipated due to the carbon/defects at the grain boundaries. Low-temperature post-processing, such as plasma treatment, could be explored to reduce/clean the residual carbon to enhance the electrical, optical, and mechanical properties. Besides post-processing techniques, nanocrystals capped with shorter ligands (than oleylamine) will be prepared and printed to reduce the carbon content in the resultants.

#### EXPERIMENTAL SECTION AND METHODS

Oleylamine-Capped Nanocrystal Preparation. Oleylamine (OA)-capped gold nanocrystals (3-4 nm particle size, UTDAu25X) were obtained from UTdots. The same OA-capped nanocrystals were also prepared in-house following the published synthesis process, as described in the following: 0.4456 g of gold(III) chloride trihydrate was dissolved in 2.285 mL of oleylamine and 8.285 mL of toluene under vigorous stirring to create the metal/amine complex. The complex was kept under stirring for 10 min before the reducing agent was injected. Separately, 0.044 g of sodium borohydride was dissolved in 10 mL of 200 proof ethanol to create the reducing agent. The reducing agent was pumped at 0.143 mL/min into the metal/amine complex. The total reaction time was 56 min. After the reaction, the solution was kept stirring for 60 min. The nanocrystals were precipitated and purified using methanol, cleaned with ethanol, and dried for use. The nanoparticle ink was prepared by dissolving the dry particles in solvents such as xylene or terpineol. Similar properties and printing behaviors were confirmed between commercial and synthesized inks.

Femtosecond Laser-Printing System. A femtosecond pulsed laser (Calmar Cazadero) with 1030 nm wavelength, ~700 fs pulse width, and adjustable repetition rates (120 KHz–27 MHz) was used in this process. The laser beam was expanded by a beam expander before being focused by a high numerical aperture oil immersion objective (Olympus UPLFLN40XO with NA = 1.3). A sealed chamber was prepared containing OA-capped gold nanocrystal ink (0.2 wt % in solvents such as xylene and terpineol). The chamber was then mounted on a three-axis piezoelectric stage.

Preparation of the Interfacial Layer and the Printing Chamber. The Laurell WS 650-23B spin coater was used to perform the spinning process. First, a regular glass slide was cut into smaller pieces and cleaned with different solvents including acetone, ethanol, isopropanol, and deionized water. Highly concentrated (25 wt %) commercial oleylamine-capped gold nanocrystal ink in xylene was then spin-coated on the cleaned glass substrates. A 2000 rpm 45 s spinning program was set to perform this process. A sealed chamber was prepared to contain the diluted nanocrystal ink and to prevent it from drying out during printing. A commercial Imaging spacer (SecureSeal 654004, Grace Bio Labs) with the 0.12 mm thickness was mounted on the substrate with the spin-coated interfacial layer. Twothree drops of the 0.2 wt % of nanocrystal ink (commercial or synthesized nanocrystals dissolved in solvents) were placed at the center of the spacer area. The solvent is typically xylene. Terpineol is also introduced with a predetermined volume ratio to adjust the viscosity of the solvent when needed. Finally, a regular coverslip (0.17 mm thick) was placed and pressed on top to make the whole chamber sealed properly. The chamber was mounted carefully on a regular glass slide with a double-sided tape to keep it fixed during the printing process and stage movements.

Characterization of the Printed Structures. All of the SEM images were captured using a scanning electron microscope (Hitachi S4700 FESEM). A transmission electron microscope (Tecnai F20 TEM) was used to capture the TEM images. Raman measurements were carried out using a Renishaw InVia Raman microscope with a 633 nm HeNe laser as the excitation source.

#### ASSOCIATED CONTENT

## Supporting Information

The Supporting Information is available free of charge at https://pubs.acs.org/doi/10.1021/acsami.1c10775.

Laser printing pillar array (MP4)

Laser printing 3D free-standing hierarchical structure (MP4)

Comparison of submicron, direct, and scalable metal 3D printing techniques based on geometric complexity of printing, electrical conductivity, and substrate constraints (Table S1); parameters used in the three-temperature (3-T) model (Table S2); SEM image of 3D structures subjected to thermal annealing at various temperatures and measured resistance (Figure S1); SEM image of 2D structures used for measured electrical conductivity (Figure S2); electron diffraction pattern of laser-printed gold structures. (Figure S3); measured pulse duration/width by autocorrelation (Figure S4); optical transmission is monitored in situ as NC deposited/printed on the substrate (Figure S5) (PDF)

## AUTHOR INFORMATION

### **Corresponding Author**

Heng Pan − J. Mike Walker '66 Department of Mechanical Engineering, Texas A&M University, College Station, Texas 77843, United States; Department of Mechanical and Aerospace Engineering, Missouri University of Science and Technology, Rolla, Missouri 65401, United States; orcid.org/0000-0003-4877-127X; Email: hpan@tamu.edu, hp5c7@mst.edu

#### **Authors**

Chinmoy Podder – J. Mike Walker '66 Department of Mechanical Engineering, Texas A&M University, College Station, Texas 77843, United States

Xiangtao Gong – J. Mike Walker '66 Department of Mechanical Engineering, Texas A&M University, College Station, Texas 77843, United States

Xiaowei Yu - Department of Mechanical and Aerospace Engineering, Missouri University of Science and Technology, Rolla, Missouri 65401, United States; ⊙ orcid.org/0000-0002-5024-9029

Wan Shou – Department of Mechanical and Aerospace Engineering, Missouri University of Science and Technology, Rolla, Missouri 65401, United States

Complete contact information is available at: https://pubs.acs.org/10.1021/acsami.1c10775

# **Funding**

National Science Foundation under Grant no. 2054104 (1635256) and no. 2054098 (1846673).

#### Notes

The authors declare no competing financial interest.

# ACKNOWLEDGMENTS

This work is supported by the National Science Foundation under Grant no. 2054104 (1635256) and no. 2054098 (1846673). The financial supports are greatly appreciated.

## REFERENCES

(1) Woodfield, T. B. F.; Malda, J.; de Wijn, J.; Peters, F.; Riesle, J.; van Blitterswijk, C. A. Design of Porous Scaffolds for Cartilage Tissue

- Engineering Using a Three-Dimensional Fiber-Deposition Technique. *Biomaterials* **2004**, *25*, 4149–4161.
- (2) Liu, R.; Wang, Z.; Sparks, T.; Liou, F.; Newkirk, J. Aerospace Applications of Laser Additive Manufacturing. *Woodhead Publ. Ser. Electron. Opt. Mater.* **2017**, *88*, 351–371.
- (3) Vaezi, M.; Seitz, H.; Yang, S. F. A Review on 3d Micro-Additive Manufacturing Technologies. *Int. J. Adv. Manuf. Technol.* **2013**, *67*, 1721–1754.
- (4) Maruo, S.; Kawata, S. Two-Photon-Absorbed near-Infrared Photopolymerization for Three-Dimensional Microfabrication. *J. Microelectromech. Syst.* **1998**, *7*, 411–415.
- (5) Smay, J. E.; Gratson, G. M.; Shepherd, R. F.; Cesarano, J.; Lewis, J. A. Directed Colloidal Assembly of 3d Periodic Structures. *Adv. Mater.* **2002**, *14*, 1279–1283.
- (6) Barton, K.; Mishra, S.; Shorter, K. A.; Alleyne, A.; Ferreira, P.; Rogers, J. A Desktop Electrohydrodynamic Jet Printing System. *Mechatronics* **2010**, *20*, *6*11–*6*16.
- (7) Galliker, P.; Schneider, J.; Eghlidi, H.; Kress, S.; Sandoghdar, V.; Poulikakos, D. Direct Printing of Nanostructures by Electrostatic Autofocussing of Ink Nanodroplets. *Nat. Commun.* **2012**, *3*, No. 890.
- (8) Ahn, B. Y.; Duoss, E. B.; Motala, M. J.; Guo, X. Y.; Park, S. I.; Xiong, Y. J.; Yoon, J.; Nuzzo, R. G.; Rogers, J. A.; Lewis, J. A. Omnidirectional Printing of Flexible, Stretchable, and Spanning Silver Microelectrodes. *Science* **2009**, 323, 1590–1593.
- (9) Hu, J.; Yu, M. F. Meniscus-Confined Three-Dimensional Electrodeposition for Direct Writing of Wire Bonds. *Science* **2010**, 329, 313–316.
- (10) Gissibl, T.; Thiele, S.; Herkommer, A.; Giessen, H. Sub-Micrometre Accurate Free-Form Optics by Three-Dimensional Printing on Single-Mode Fibres. *Nat. Commun.* **2016**, *7*, No. 11763.
- (11) Yu, C.; Schimelman, J.; Wang, P. R.; Miller, K. L.; Ma, X. Y.; You, S. T.; Guan, J. A.; Sun, B. J.; Zhu, W.; Chen, S. C. Photopolymerizable Biomaterials and Light-Based 3d Printing Strategies for Biomedical Applications. *Chem. Rev.* **2020**, *120*, 10748–10796.
- (12) Cooperstein, I.; Indukuri, S. R. K. C.; Bouketov, A.; Levy, U.; Magdassi, S. 3d Printing of Micrometer-Sized Transparent Ceramics with on-Demand Optical-Gain Properties. *Adv. Mater.* **2020**, *32*, No. 2001675.
- (13) Park, S.; Lee, D. H.; Ryoo, H. I.; Lim, T. W.; Yang, D. Y.; Kim, D. P. Fabrication of Three-Dimensional Sic Ceramic Microstructures with near-Zero Shrinkage Via Dual Crosslinking Induced Stereo-lithography. *Chem. Commun.* **2009**, *32*, 4880–4882.
- (14) Passinger, S.; Saifullah, M. S. M.; Reinhardt, C.; Subramanian, K. R. V.; Chichkov, B. N.; Welland, M. E. Direct 3d Patterning of Tio2 Using Femtosecond Laser Pulses. *Adv. Mater.* **200**7, *19*, 1218–1221.
- (15) Bertsch, A.; Jiguet, S.; Renaud, P. Microfabrication of Ceramic Components by Microstereolithography. *J. Micromech. Microeng.* **2004**, *14*, 197–203.
- (16) Kim, K.; Zhu, W.; Qu, X.; Aaronson, C.; McCall, W. R.; Chen, S. C.; Sirbuly, D. J. 3d Optical Printing of Piezoelectric Nanoparticle Polymer Composite Materials. *ACS Nano* **2014**, *8*, 9799–9806.
- (17) Xu, B. B.; Zhang, Y. L.; Zhang, R.; Wang, L.; Xiao, X. Z.; Xia, H.; Chen, Q. D.; Sun, H. B. Programmable Assembly of Cdte Quantum Dots into Microstructures by Femtosecond Laser Direct Writing. J. Mater. Chem. C 2013, 1, 4699–4704.
- (18) Cohen, A.; Zhang, G.; Tseng, F. G.; Mansfeld, F.; Frodis, U.; Will, P. Efab: Batch Production of Functional Fully-Dense Metal Parts with Micron-Scale Features. *Sol. Freeform Fabr.* 1998, 161–168.
- (19) Sekitani, T.; Noguchi, Y.; Zschieschang, U.; Klauk, H.; Someya, T. Organic Transistors Manufactured Using Inkjet Technology with Subfemtoliter Accuracy. *Proc. Natl. Acad. Sci. U.S.A.* **2008**, *105*, 4976–4980
- (20) Fukuda, K.; Takeda, Y.; Yoshimura, Y.; Shiwaku, R.; Tran, L. T.; Sekine, T.; Mizukami, M.; Kumaki, D.; Tokito, S. Fully-Printed High-Performance Organic Thin-Film Transistors and Circuitry on One-Micron-Thick Polymer Films. *Nat. Commun.* **2014**, No. 4147.

- (21) Felton, S.; Tolley, M.; Demaine, E.; Rus, D.; Wood, R. A Method for Building Self-Folding Machines. *Science* **2014**, *345*, 644–646.
- (22) Zhou, L.; Tan, Y. L.; Wang, J. Y.; Xu, W. C.; Yuan, Y.; Cai, W. S.; Zhu, S. N.; Zhu, J. 3d Self-Assembly of Aluminium Nanoparticles for Plasmon-Enhanced Solar Desalination. *Nat. Photonics* **2016**, *10*, 393–398.
- (23) Khorasaninejad, M.; Chen, W. T.; Devlin, R. C.; Oh, J.; Zhu, A. Y.; Capasso, F. Metalenses at Visible Wavelengths: Diffraction-Limited Focusing and Subwavelength Resolution Imaging. *Science* **2016**, 352, 1190–1194.
- (24) Xu, L. Z.; Gutbrod, S. R.; Bonifas, A. P.; Su, Y. W.; Sulkin, M. S.; Lu, N. S.; Chung, H. J.; Jang, K. I.; Liu, Z. J.; Ying, M.; Lu, C.; Webb, R. C.; Kim, J. S.; Laughner, J. I.; Cheng, H. Y.; Liu, Y. H.; Ameen, A.; Jeong, J. W.; Kim, G. T.; Huang, Y. G.; Efimov, I. R.; Rogers, J. A. 3d Multifunctional Integumentary Membranes for Spatiotemporal Cardiac Measurements and Stimulation across the Entire Epicardium. *Nat. Commun.* 2014, 5, No. 3329.
- (25) He, B.; Yang, Y.; Yuen, M. F.; Chen, X. F.; Lee, C. S.; Zhang, W. J. Vertical Nanostructure Arrays by Plasma Etching for Applications in Biology, Energy, and Electronics. *Nano Today* **2013**, *8*, 265–289.
- (26) Lis, D.; Caudano, Y.; Henry, M.; Demoustier-Champagne, S.; Ferain, E.; Cecchet, F. Selective Plasmonic Platforms Based on Nanopillars to Enhance Vibrational Sum-Frequency Generation Spectroscopy. *Adv. Opt. Mater.* **2013**, *1*, 244–255.
- (27) Nesbitt, N. T.; Naughton, M. J. A Review: Methods to Fabricate Vertically Oriented Metal Nanowire Arrays. *Ind. Eng. Chem. Res.* **2017**, *56*, 10949–10957.
- (28) Hai, A.; Shappir, J.; Spira, M. E. In-Cell Recordings by Extracellular Microelectrodes. *Nat. Methods* **2010**, *7*, 200–202.
- (29) Wu, S. M.; Zuber, F.; Brugger, J.; Maniura-Weber, K.; Ren, Q. Antibacterial Au Nanostructured Surfaces. *Nanoscale* **2016**, *8*, 2620–2625.
- (30) Higgins, S. G.; Becce, M.; Belessiotis-Richards, A.; Seong, H.; Sero, J. E.; Stevens, M. M. High-Aspect-Ratio Nanostructured Surfaces as Biological Metamaterials. *Adv. Mater.* **2020**, 32, No. 1903862.
- (31) Kullmann, C.; Schirmer, N. C.; Lee, M. T.; Ko, S. H.; Hotz, N.; Grigoropoulos, C. P.; Poulikakos, D. 3d Micro-Structures by Piezoelectric Inkjet Printing of Gold Nanofluids. *J. Micromech. Microeng.* **2012**, *22*, No. 055022.
- (32) Saleh, M. S.; Hu, C. S.; Panat, R. Three-Dimensional Microarchitected Materials and Devices Using Nanoparticle Assembly by Pointwise Spatial Printing. *Sci. Adv.* **2017**, *3*, No. e1601986.
- (33) Baeuerle, D. Perspectives of Laser Processing and Chemistry. *Proc. Soc. Photo-Opt. Instrum. Eng.* **2002**, 4760, 11–18.
- (34) Skylar-Scott, M. A.; Gunasekaran, S.; Lewis, J. A. Laser-Assisted Direct Ink Writing of Planar and 3d Metal Architectures. *Proc. Natl. Acad. Sci. U.S.A.* **2016**, *113*, 6137–6142.
- (35) Wang, J. W.; Auyeung, R. C. Y.; Kim, H.; Charipar, N. A.; Pique, A. Three-Dimensional Printing of Interconnects by Laser Direct-Write of Silver Nanopastes. *Adv. Mater.* **2010**, *22*, 4462–4466.
- (36) Piqué, A.; Auyeung, R. C. Y.; Kim, H.; Metkus, K. M.; Mathews, S. A. Digital Microfabrication by Laser Decal Transfer. *J. Laser Micro/Nanoeng.* **2008**, *3*, 163–169.
- (37) Zenou, M.; Sa'ar, A.; Kotler, Z. Laser Transfer of Metals and Metal Alloys for Digital Microfabrication of 3d Objects. *Small* **2015**, 11, 4082–4089.
- (38) Visser, C. W.; Pohl, R.; Sun, C.; Roemer, G. W.; in 't Veld, B. H.; Lohse, D. Toward 3d Printing of Pure Metals by Laser-Induced Forward Transfer. *Adv. Mater.* **2015**, *27*, 4087–4092.
- (39) Takai, T.; Nakao, H.; Iwata, F. Three-Dimensional Microfabrication Using Local Electrophoresis Deposition and a Laser Trapping Technique. *Opt. Express* **2014**, 22, 28109–28117.
- (40) Suryavanshi, A. P.; Yu, M. F. Probe-Based Electrochemical Fabrication of Freestanding Cu Nanowire Array. *Appl. Phys. Lett.* **2006**, *88*, No. 083103.

- (41) Hirt, L.; Ihle, S.; Pan, Z. J.; Dorwling-Carter, L.; Reiser, A.; Wheeler, J. M.; Spolenak, R.; Voros, J.; Zambelli, T. Template-Free 3d Microprinting of Metals Using a Force-Controlled Nanopipette for Layer-by-Layer Electrodeposition. *Adv. Mater.* **2016**, 28, 2311–2315.
- (42) Utke, I.; Hoffmann, P.; Melngailis, J. Gas-Assisted Focused Electron Beam and Ion Beam Processing and Fabrication. J. Vac. Sci. Technol., B: Microelectron. Nanometer Struct.—Process., Meas., Phenom. 2008, 26, 1197—1276.
- (43) Tanaka, T.; Ishikawa, A.; Kawata, S. Two-Photon-Induced Reduction of Metal Ions for Fabricating Three-Dimensional Electrically Conductive Metallic Microstructure. *Appl. Phys. Lett.* **2006**, *88*, No. 081107.
- (44) Shukla, S.; Furlani, E. P.; Vidal, X.; Swihart, M. T.; Prasad, P. N. Two-Photon Lithography of Sub-Wavelength Metallic Structures in a Polymer Matrix. *Adv. Mater.* **2010**, *22*, 3695–3699.
- (45) Barton, P.; Mukherjee, S.; Prabha, J.; Boudouris, B. W.; Pan, L.; Xu, X. F. Fabrication of Silver Nanostructures Using Femtosecond Laser-Induced Photoreduction. *Nanotechnology* **2017**, 28, No. 505302.
- (46) Cao, Y. Y.; Takeyasu, N.; Tanaka, T.; Duan, X. M.; Kawata, S. 3d Metallic Nanostructure Fabrication by Surfactant-Assisted Multiphoton-Induced Reduction. *Small* **2009**, *5*, 1144–1148.
- (47) Blasco, E.; Muller, J.; Muller, P.; Trouillet, V.; Schon, M.; Scherer, T.; Barner-Kowollik, C.; Wegener, M. Fabrication of Conductive 3d Gold-Containing Microstructures Via Direct Laser Writing. *Adv. Mater.* **2016**, *28*, 3592–3595.
- (48) Ishikawa, A.; Tanakaa, T.; Kawata, S. Improvement in the Reduction of Silver Ions in Aqueous Solution Using Two-Photon Sensitive Dye. *Appl. Phys. Lett.* **2006**, *89*, No. 113102.
- (49) Vyatskikh, A.; Delalande, S.; Kudo, A.; Zhang, X.; Portela, C. M.; Greer, J. R. Additive Manufacturing of 3d Nano-Architected Metals. *Nat. Commun.* **2018**, *9*, No. 593.
- (50) Ko, S. H.; Pan, H.; Grigoropoulos, C. P.; Luscombe, C. K.; Frechet, J. M. J.; Poulikakos, D. Air Stable High Resolution Organic Transistors by Selective Laser Sintering of Ink-Jet Printed Metal Nanoparticles. *Appl. Phys. Lett.* **2007**, *90*, No. 141103.
- (51) Bieri, N. R.; Chung, J.; Haferl, S. E.; Poulikakos, D.; Grigoropoulos, C. P. Microstructuring by Printing and Laser Curing of Nanoparticle Solutions. *Appl. Phys. Lett.* **2003**, *82*, 3529–3531.
- (52) Theodorakos, I.; Zacharatos, F.; Geremia, R.; Karnakis, D.; Zergioti, I. Selective Laser Sintering of Ag Nanoparticles Ink for Applications in Flexible Electronics. *Appl. Surf. Sci.* **2015**, 336, 157–162.
- (53) Son, Y.; Yeo, J.; Moon, H.; Lim, T. W.; Hong, S.; Nam, K. H.; Yoo, S.; Grigoropoulos, C. P.; Yang, D. Y.; Ko, S. H. Nanoscale Electronics: Digital Fabrication by Direct Femtosecond Laser Processing of Metal Nanoparticles. *Adv. Mater.* **2011**, 23, 3176–3181.
- (54) Pan, H.; Hwang, D. J.; Ko, S. H.; Clem, T. A.; Frechet, J. M. J.; Bauerle, D.; Grigoropoulos, C. P. High-Throughput near-Field Optical Nanoprocessing of Solution-Deposited Nanoparticles. *Small* **2010**, *6*, 1812–1821.
- (55) Salaita, K.; Lee, S. W.; Wang, X. F.; Huang, L.; Dellinger, T. M.; Liu, C.; Mirkin, C. A. Sub-100 Nm, Centimeter-Scale, Parallel Dip-Pen Nanolithography. *Small* **2005**, *1*, 940–945.
- (56) Palazon, F.; Prato, M.; Manna, L. Writing on Nanocrystals: Patterning Colloidal Inorganic Nanocrystal Films through Irradiation-Induced Chemical Transformations of Surface Ligands. *J. Am. Chem. Soc.* **2017**, *139*, 13250–13259.
- (57) Yamada, T.; Fukuhara, K.; Matsuoka, K.; Minemawari, H.; Tsutsumi, J.; Fukuda, N.; Aoshima, K.; Arai, S.; Makita, Y.; Kubo, H.; Enomoto, T.; Togashi, T.; Kurihara, M.; Hasegawa, T. Nanoparticle Chemisorption Printing Technique for Conductive Silver Patterning with Submicron Resolution. *Nat. Commun.* **2016**, *7*, No. 11402.
- (58) Shou, W.; Pan, H. Direct Printing of Microstructures by Femtosecond Laser Excitation of Nanocrystals in Solution. *Appl. Phys. Lett.* **2016**, *108*, No. 214101.
- (59) Wang, Y. Y.; Fedin, I.; Zhang, H.; Talapin, D. V. Direct Optical Lithography of Functional Inorganic Nanomaterials. *Science* **2017**, 357, 385–388.

- (60) Mourdikoudis, S.; Liz-Marzan, L. M. Oleylamine in Nanoparticle Synthesis. *Chem. Mater.* **2013**, 25, 1465–1476.
- (61) Chiang, W. Y.; Okuhata, T.; Usman, A.; Tamai, N.; Masuhara, H. Efficient Optical Trapping of Cdte Quantum Dots by Femtosecond Laser Pulses. *J. Phys. Chem. B* **2014**, *118*, 14010–14016.
- (62) Jauffred, L.; Richardson, A. C.; Oddershede, L. B. Three-Dimensional Optical Control of Individual Quantum Dots. *Nano Lett.* **2008**, *8*, 3376–3380.
- (63) Saalfrank, P. Quantum Dynamical Approach to Ultrafast Molecular Desorption from Surfaces. *Chem. Rev.* **2006**, *106*, 4116–4159
- (64) Simoncelli, S.; Li, Y.; Cortes, E.; Maier, S. A. Nanoscale Control of Molecular Self-Assembly Induced by Plasmonic Hot-Electron Dynamics. *ACS Nano* **2018**, *12*, 2184–2192.
- (65) Logunov, S. L.; Ahmadi, T. S.; ElSayed, M. A.; Khoury, J. T.; Whetten, R. L. Electron Dynamics of Passivated Gold Nanocrystals Probed by Subpicosecond Transient Absorption Spectroscopy. *J. Phys. Chem. B* **1997**, *101*, 3713–3719.
- (66) Guzelturk, B.; Utterback, J. K.; Coropceanu, I.; Kamysbayev, V.; Janke, E. M.; Zajac, M.; Yazdani, N.; Cotts, B. L.; Park, S.; Sood, A.; Lin, M. F.; Reid, A. H.; Kozina, M. E.; Shen, X. Z.; Weathersby, S. P.; Wood, V.; Salleo, A.; Wang, X. J.; Talapin, D. V.; Ginsberg, N. S.; Lindenberg, A. M. Nonequilibrium Thermodynamics of Colloidal Gold Nanocrystals Monitored by Ultrafast Electron Diffraction and Optical Scattering Microscopy. ACS Nano 2020, 14, 4792–4804.
- (67) Aruda, K. O.; Tagliazucchi, M.; Sweeney, C. M.; Hannah, D. C.; Schatz, G. C.; Weiss, E. A. Identification of Parameters through Which Surface Chemistry Determines the Lifetimes of Hot Electrons in Small Au Nanoparticles. *Proc. Natl. Acad. Sci. U.S.A.* **2013**, *110*, 4212–4217.